Available online at www.sciencedirect.com
ScienceDirect
Trans. Nonferrous Met. Soc. China 33(2023) 2231−2244
Transactions of Nonferrous Metals Society of China
www.tnmsc.cn

Numerical modelling of stirring characteristics of gas−slag−copper matte multiphase flow in bath with top submerged lance

Zhang-hao WAN[1], Shi-liang YANG[1], De-song KONG[2], Dong-bo LI[2], Jian-hang HU[1], Hua WANG[1]

1. State Key Laboratory of Complex Nonferrous Metal Resources Clean Utilization, Kunming University of Science and Technology, Kunming 650093, China;
2. Southwest Copper Branch, Yunnan Copper Co., Ltd., Kunming 650102, China

Received 5 March 2022; accepted 8 June 2022

Abstract: The hydrodynamics and stirring characteristics of the nitrogen−slag−copper matte in a bath with top submerged lance were numerically studied via the volume-of-fluid (VOF) method. The relationship between the bubble behavior and fluid velocity was elucidated. The effects of gas injecting velocity and swirling flow on the fluid vortex structure, gas penetration depth, and fluid velocity were investigated. The results demonstrate that the formation and rising of the bubble increase and reduce the fluid velocity, respectively. The V-shaped and W-shaped temperature distributions of the fluid are observed at the height of 0.43 and 0.52 m, respectively, resulting from the injection of the low-temperature gas phase. Compared to the gas injection velocity of 58 m/s, the time-averaged and maximum penetration depths of the gas phase with the injection velocity of 96 m/s increase by 78.4 % and 31.9 %, respectively. Swirling flow reduces the gas penetration depth, enhances the momentum transfer efficiency between phases, and suppresses the slag splashing, which is attributed to the reduced axial velocity component.

Key words: top submerged lance; bubble behavior; swirling flow; multiphase flow; nitrogen−slag−copper matte

1 Introduction

The gas−liquid multiphase mixing flow is prevalently involved in the metallurgical process, petrochemical process, wastewater treatment, and other applications [1−4]. Traditionally, it can be divided into the liquid injection into gas in the form of droplets [5], and gas injection into the liquid in the form of bubbles [6,7]. The top submerged injection process, which has numerous attractive features including excellent gas−liquid contact efficiency, no mechanical stirring requirement and precise operation [8−10], is a typical method for driving liquid to move via gas injected to the high-temperature molten slag.

During the top submerged injection process, the stirring of bubbles to the liquid influences the gas−liquid mixing performance and the liquid splashing volume. The hydrodynamics during the stirring process in the top submerged lance (TSL) reactor should be deeply studied. Until now, numerous experiments have been carried out with a laboratory-scale cold air−water test rig to replace the high-temperature industrial reaction system due to the harsh operating conditions and opaque nature of measurement instruments of the commercial furnace [11]. The results showed that the bubble behavior and gas−liquid dispersion are impacted by gas injector structure (e.g., orifice type, diameter, and designing location) [12], operating parameters (e.g., gas flow rate, submergence depth of lance and injection layout arrangement), liquid properties (e.g., density and viscosity) [13] and interaction force between phases (e.g., buoyancy drag and surface tension) [14,15]. AKASHI et al [16] found

Corresponding author: Shi-liang YANG, Fax: +86-871-5153405, E-mail: yangshiliang0802@163.com
DOI: 10.1016/S1003-6326(23)66255-7

that rising bubbles drive liquid to move and induce the recirculating flow of the liquid. Increasing the lance immersion depth enhances the stability of the flow pattern. LIOW et al [17] experimentally observed that the bubble formation is initially controlled by the diameter of the inner lance. When the maximum bubble pressure exceeds the critical value, the formation of the bubble is governed by intermediate diameters between the inner and outer lances. However, in the experimental investigations, understanding the multiphase mixing in the complex structure is limited to the macroscopic information of the flow field. A comprehensive study of the momentum transfer process is far from well understood.

With the development of the computer algorithm and hardware, the computational fluid dynamic (CFD) method provides a useful and cost-effective way to extract results that are hardly captured in the experimental investigations, thereby realizing the goals of visualizing the in-furnace phenomenon and improving energy efficiency. WANG et al [18] studied the effects of the oil−gas velocity ratio (the ratio of oil injection velocity to gas injection velocity) on the flow pattern and turbulent kinetic energy distribution in a three-dimension (3-D) gas−liquid mixing reactor via the volume-to-fluid (VOF) method. The results indicated that the oil−gas slug flow is formed due to the tangential force from the gas to the oil phase, and the bubble width increases when the oil−gas velocity ratio varies from 0 to 2 but reduces when the oil−gas ratio is larger than 2. OBISO et al [19] used the VOF model to predict the bubble detachment frequency and dynamics of gas−liquid multiphase flow. The results confirmed that a sloshing wave can be observed in the top configuration with a frequency of 2 Hz. The perfectly symmetric profile and asymmetric step of the free surface were presented with an increase in lance submerged depth. Nevertheless, the flow characteristics obtained in the cold test rig are not completely applicable to the industrial mixing process of ternary fluid due to the large discrepancy in the fluid properties between the isothermal lab-scale vessel and high-temperature industrial-scale reactor. Moreover, the spatial distribution of gas vortex, and bubble aspect ratio for evaluating the agitation intensity are rarely documented in the CFD modeling for the TSL process.

To fulfill the gap, numerical simulation via the VOF approach is conducted in this work to investigate the flow hydrodynamics of the bubble and the nitrogen−slag−matte three-phase stirring process in the TSL reactor. Specifically, the properties of the ternary mixture in this work are set according to the industrial parameters. Firstly, the grid independence is tested regarding the time that the bubble rises to the molten slag surface, and the numerical model is validated via the bubble morphology. Subsequently, space−time evolution of the fluid velocity and bubble behaviors are investigated. Furthermore, the impacts of several vital operating parameters (e.g., gas flow rate, and swirling flow) on the spatial distribution of the Q-criterion and the time-averaged velocity plots are discussed.

2 Numerical methods

In the present study, the VOF model, which is solved under the Eulerian framework, is utilized to give a quantitative analysis of the hydrodynamics in the TSL reactor due to its high precision for reconstructing the interfaces among the immiscible fluids. In this approach, the coexistence of different phases in the individual cell is adopted but the miscibility between the multiphase is disapproved. The advanced interface-tracking method, named explicit geometric reconstruction scheme, is employed to distinctly capture the interface position of the non-miscible phases through applying a piecewise linear special interpolation treatment to a cell near the interface [20]. The volume fraction (α_i) of each filling fluid is considered to identify the underlying fluid phases per unit volume, and the sum of the volume fractions of the phases is 1 ($\sum_i \alpha_i = 1$).

In the VOF model, both the gas and liquid phases are considered as the continuous phases and solved via a single-fluid formulation in the computational domain, indicating that the variables (e.g., velocity fields, and pressure fields) and properties (e.g., density, and viscosity) in each cell are shared by all phases. The mass and momentum equations for the fluid phase are established as follows:

$$\frac{\partial}{\partial t}(\rho) + \nabla \cdot \rho \boldsymbol{u} = 0 \tag{1}$$

$$\frac{\partial}{\partial t}(\rho \boldsymbol{u}) + \nabla \cdot (\rho \boldsymbol{u}\boldsymbol{u}) = -\nabla p + \rho \boldsymbol{g} + \nabla \cdot [\mu(\nabla \boldsymbol{u} + \nabla \boldsymbol{u}^{\mathrm{T}})] + \boldsymbol{F}_{\mathrm{ST}} \quad (2)$$

where ρ, $\boldsymbol{u}$, p and μ represent the fluid density, velocity, pressure, and molecular viscosity, respectively; t and $\boldsymbol{g}$ are the instant time and gravitational acceleration, respectively; $\boldsymbol{F}_{\mathrm{ST}}$ denotes the surface tension force between the phases in the computational grid. To capture the interface of the nitrogen−slag−matte three phases, the formulation of the void fraction is solved and depicted as follows:

$$\frac{\partial \alpha}{\partial t} + \nabla(\alpha \boldsymbol{u}) = 0 \quad (3)$$

Here, the volume fraction varies between 0 and 1. Since immiscible phases coexist in the domain, the density and viscosity of the multiphase mixture are given as follows:

$$\alpha_{1\mathrm{st}} + \alpha_{2\mathrm{nd}} + \alpha_{3\mathrm{rd}} = 1 \quad (4)$$

$$\rho = \alpha_{1\mathrm{st}}\rho_{1\mathrm{st}} + \alpha_{2\mathrm{nd}}\rho_{2\mathrm{nd}} + \alpha_{3\mathrm{rd}}\rho_{3\mathrm{rd}} \quad (5)$$

$$\mu = \alpha_{1\mathrm{st}}\mu_{1\mathrm{st}} + \alpha_{2\mathrm{nd}}\mu_{2\mathrm{nd}} + \alpha_{3\mathrm{rd}}\mu_{3\mathrm{rd}} \quad (6)$$

where $\alpha_{1\mathrm{st}}$, $\alpha_{2\mathrm{nd}}$ and $\alpha_{3\mathrm{rd}}$ represent the volume fraction of the primary phase, second phase, and third phase, respectively.

The heat transfer between the gas−liquid phases is taken into account via the energy conservation equation:

$$\frac{\partial}{\partial t}(\rho E) + \nabla \cdot [\boldsymbol{u}(\rho E + p)] = \nabla \cdot (k_{\mathrm{eff}} \nabla T) + S_{\mathrm{h}} \quad (7)$$

where k_{eff} and T represent the effective thermal conductivity and temperature, respectively. The energy source term, S_{h}, comprises the volumetric heat sources and energy transfer from radiation.

In the VOF method, the fluid energy (E) is defined as a mass-averaged variable:

$$E = \frac{\sum_{q=1}^{n} \alpha_q \rho_q E_q}{\sum_{q=1}^{n} \alpha_q \rho_q} \quad (8)$$

$$E_q = h_q - \frac{p}{\rho_q} + \frac{\boldsymbol{u}^2}{2} \quad (9)$$

where h_q stands for the fluid enthalpy. The enthalpy for each phase is based on the specific heat of that phase and shared temperature.

The surface tension force, which dominates the flow pattern of the immiscible flow as a volume force [21], is considered via the continuum surface force (CSF) model proposed by BRACKBILL et al [22]:

$$\boldsymbol{F}_{\mathrm{ST}} = \sum_{\mathrm{pairsij},i<j} \sigma_{ij} \frac{\alpha_i \rho_i k_j \nabla \alpha_j + \alpha_j \rho_j k_i \nabla \alpha_i}{0.5(\rho_i + \rho_j)} \quad (10)$$

Besides the conservation equations of fluid, the shear stress transport (SST) k-omega two-equation model, which comprises the turbulence kinetic energy (k) equation and eddy dissipation rate (ω) equation, provides the turbulence closure for the continuous phase. The formulations of k and ω based on the k–ε dispersed turbulence model are formulated as follows [23]:

$$\frac{\partial}{\partial t}(\rho k) + \frac{\partial k}{\partial x_j}(\rho k u_j) = P_k - \rho \beta_* k\omega + \frac{\partial}{\partial x_j}\left[\frac{\partial}{\partial x_j}\left(k\left((\mu + \frac{\mu_{\mathrm{t}}}{\sigma_k})\right)\right)\right] \quad (11)$$

$$\frac{\partial}{\partial t}(\rho \omega) + \frac{\partial}{\partial x_j}(\rho \omega u_j) = \alpha P_\omega - \rho \beta \omega^2 + \frac{\partial}{\partial x_j}\left[\frac{\partial}{\partial x_j}\left(\omega\left(\mu + \frac{\mu_{\mathrm{t}}}{\sigma_\omega}\right)\right)\right] + 2\rho(1 - F_1)\sigma_{\omega 2}\frac{1}{\omega}\frac{\partial k}{\partial x_i}\frac{\partial \omega}{\partial x_j} \quad (12)$$

where β_* is a closure coefficient in the turbulence model with a value of 0.09, and the blending function β is given in Eq. (13). σ_k and σ_ω represent the turbulent Prandtl numbers for k and ω, respectively. The x_i and x_j denote the grid positions. The symbol μ_{t} is the turbulent viscosity expressed in Eq. (14):

$$\beta = \beta_1 F_1 + \beta_2(1 - F_1) \quad (13)$$

$$\mu_{\mathrm{t}} = \frac{\rho k}{\omega}\frac{1}{\max(\frac{1}{\alpha^*}, \frac{SF_2}{a_1 \omega})} \quad (14)$$

Here, a_1 is an experimental constant with a value of 0.31. S is the magnitude of the strain rate and is given in Eq. (15). The formulations of the α^* and F_2 are established as

$$S = \sqrt{2S_{ij}S_{ij}} \quad (15)$$

$$\alpha^* = \alpha_\infty^* \left(\frac{\alpha_0^* + Re_t/R_k}{1 + Re_t/R_k} \right) \tag{16}$$

$$F_2 = \tanh\left[\left[\max\left(\frac{2\sqrt{k}}{0.09\omega y}, \frac{500\mu}{\rho\omega y^2} \right) \right]^2 \right] \tag{17}$$

where α_0^* is set as 0.024. In the high-Reynolds numbers flow, both α^* and α_∞^* are equal to 1. y represents the distance of the computational cell to the nearest surface. The formulation of the rare-of-strain S_{ij} is described by

$$S_{ij} = \frac{1}{2}\left(\frac{\partial u_j}{\partial x_i} + \frac{\partial u_i}{\partial x_j} \right) \tag{18}$$

The terms P_k and P_ω in Eqs. (11) and (12) represent the production of k and ω, respectively. The corresponding formulation of P_k, P_ω and blending function F_1 are expressed as follows:

$$P_k = -\rho\overline{u_i' u_j'} \frac{\partial u_j}{\partial x_i} \tag{19}$$

$$P_\omega = \mu_t S \tag{20}$$

$$F_1 = \tanh\left\{ \left\{ \min\left[\max\left(\frac{\sqrt{k}}{0.09\omega y}, \frac{500\mu}{\rho\omega y^2} \right), \frac{4\rho k}{\sigma_\omega D_\omega^+ y^2} \right] \right\}^4 \right\} \tag{21}$$

where D_ω^+ denotes the positive portion of cross-diffusion term and is formulated as follows:

$$D_\omega^+ = \max\left(2\rho \frac{1}{\sigma_{\omega 2}} \frac{1}{\omega} \frac{\partial k}{\partial x_i} \frac{\partial \omega}{\partial x_i}, 10^{-10} \right) \tag{22}$$

3 Computational settings

3.1 Geometry and boundary conditions

The numerical simulation is performed in a 3D cylindrical TSL reactor with a diameter of 400 mm and a height of 830 mm (Fig. 1(a)). The lance, which is utilized to supply the nitrogen, is vertically established in the middle of the reactor with a diameter of 16 mm. Two immiscible liquid species comprise the liquid layer with a total height of 520 mm and are stratified due to the density difference. Specifically, the slag phase is filled in the upper region of the liquid layer with a height of 180 mm, while the copper matte phase is filled up to a height of 340 mm in the lower region. The density and viscosity of slag and copper matte are selected according to the previous reports [24−27], and the gas is initially filled in the region above the slag surface with zero velocity. Gravitational acceleration of the fluids is considered and set as 9.81 m/s^2. The initial temperature of computational domain including the gas atmosphere, slag region, and matte region is set as 1500 K. After the ambient temperature gas is introduced from the lance to the slag phase with a fixed velocity of 67 m/s, the gas surrounds the orifice to form the bubble and then drives liquid to move. The time step of 1×10^{-5} s is utilized to accurately capture the bubble behavior. The operating parameters of the investigated reactor and the properties of the fluid are summarized in Table 1.

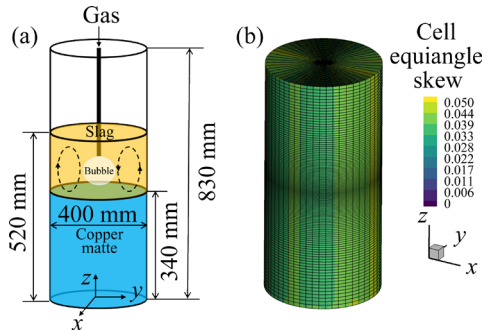

Fig. 1 Geometry (a) and grid representation (b) of investigated TSL reactor

As has been previously reported [28], the bubble morphology and motion trajectory are extremely sensitive to the grid resolution. A fine grid set required to get reasonable bubble behaviors is expensive, while the coarse grid set cannot accurately track the gas trajectory. In addition, the Reynolds number of fluid is higher near the lance than that in other regions due to the vigorous gas flow. To accurately track the gas−liquid flow with a reasonable grid number, the structured meshes with non-uniform grid sizes are considered in the turbulent regime. The selected meshes are divided into two parts by the iso-height surface of the gas inlet. The grid size of the upper part gradually increases with the height, while the grid size of the lower part decreases with the height. That is to say, a fine grid resolution is applied near the orifice because of large velocity gradients in this region, while a coarse grid resolution is adopted in other regions, as illustrated in Fig. 1(b). Specifically, the radial minimum grid size is defined near the orifice

with the value of 2 mm, and it is gradually increased to 4 mm close to the sidewall. In the vertical direction, the grid size is refined to be 2 mm due to the larger Reynolds number in the medium region of the reactor, while the maximum grid size is set to be 12 mm because of the lower Reynolds number in the upper and lower region. Finally, the total number of 310576 structured grids is selected in current work.

Table 1 Operating parameters selected in simulation

Parameter	Value or description
Reactor diameter/mm	400
Reactor height/mm	830
Lance diameter/mm	16
Initial temperature of gas and liquid region/K	1500
Height of slag phase/mm	180
Density of slag phase/(kg·m^{-3})	3500
Viscosity of slag phase/(Pa·s)	0.3
Height of copper matte phase/mm	340
Density of copper matte phase/(kg·m^{-3})	4600
Viscosity of copper matte phase/(Pa·s)	0.004
Gas species injected from orifice	Nitrogen
Gas density/(kg·m^{-3})	1.138
Gas viscosity/(Pa·s)	1.663×10^{-5}
Gas inlet velocity/(m·s^{-1})	67
Gas inlet temperature/K	300

3.2 Grid-independence test

To balance the computational accuracy and resource, the grid independence test is conducted by analyzing the time that the bubble rises to the molten slag surface. In the test only the grid size is varied, while the other parameters (e.g. grid stretching, and grid type) remain the same. Six sets of grid resolutions, i.e., 74480, 167140, 310576, 488292, 652246, and 927862 cells are utilized to perform the mesh-independence study, and the corresponding results are given in Fig. 2. The simulation results with the grid set of 310576 give an apparent discrepancy with the 74480 and 167140 grids but an insignificant change with the results of the finer grids (i.e. 488292, 652246, and 927862 cells). Thus, grid set of 310576 is chosen in the subsequent simulation of this work.

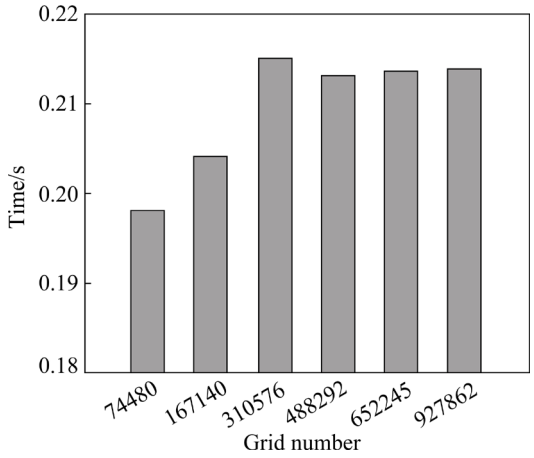

Fig. 2 Time that bubble rises to molten slag surface with different grid resolutions

4 Results and discussion

4.1 Model validation

Bubble shape and motion influence the flow regime, transfer coefficient of the heat and momentum between the gas and liquid phases. During the rising process, the bubble interacts with the surrounding liquid phase and rapidly varies its morphology, attributed to the dynamic variation of the interaction force. In this section, the simulation results of bubble behavior and the fluid velocity are compared with the experimental measurement to verify the accuracy and precision of the numerical model.

(1) Validation I: bubble rising behaviors

Firstly the bubble behavior is validated in the water model experiment, which is a rectangular box with 21.4, 21.4, and 29.4 cm in length, width, and height, respectively. The schematic diagram of the cold test rig is depicted in Fig. 3. Water is filled up to the height of 19.6 cm, which is the two-thirds of the height of the reactor. The gas is supplied from the lance with a flow rate of 1.52 L/min. In this experiment, the inner and outer diameters of the lance are 6 mm and 7 mm, respectively. Figure 4 compares the bubble morphology obtained in the experiment and simulation at different time instants. The scale bar is presented in experimental results (Figs. 4(a, c, e)). Due to the same geometric dimension as the experiment, the scale bar in the simulation results is neglected. In the numerical results, a threshold gas volume fraction of 0.5 is presented to identify the bubble boundary, as shown in Figs. 4(b, d, f). The similarity of the bubble

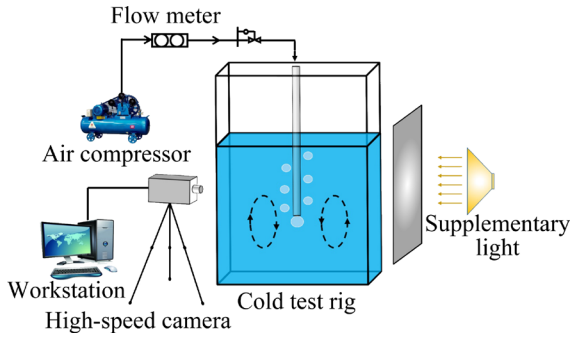

Fig. 3 Schematic diagram of cold test rig

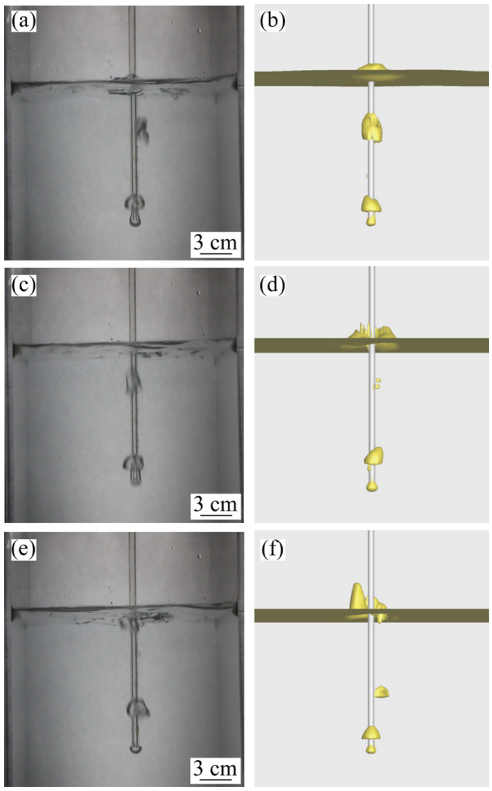

Fig. 4 Comparison of bubble motion behavior in experiment (a, c, e) and simulation (b, d, f)

morphology is observed between the experimental observation and the numerical simulations. Hemispherical bubbles are formed after the gas rushes out orifice and surrounds the outlet. During the rising process, the bubble changes to an ellipsoidal cap shape due to the combined influence of the surface tension force and buoyancy. Indeed, a slight difference between the simulation and experimental results is mainly attributed to the slight fluctuation of the gas injecting velocity and the vibration of the top submerged lance during the experiments. Furthermore, in the numerical simulation, the values of the dynamic contact angle between the bubble and lance are lacking when the bubble rises along the rim of the lance. Overall, compared to the experimental results, the bubble morphology and flow characteristics are reproduced in the simulation case, indicating the reliability of the VOF model in denoting the gas−liquid mixing flow in the TSL reactor.

(2) Validation II: velocity fields

The second validation is selected in the stable regions to reduce errors caused by the non-linear chaotic motion of the fluid and the instability of the gas injection velocity. The verification is based on the experiment conducted by MORSI et al [29] regarding the tangential velocity distribution of the fluid in the water−air system. The cylindrical tank with 230 mm in diameter and 560 mm in height is a one-sixteenth scale laboratory test rig of 150 t steel-making ladle. In line with the experimental setup, water is filled in the bottom with a height of 150 mm. Air is vertically supplied into the water with a predetermined volume flow rate (i.e., 2.67×10^{-3} m^3/s). Other details of the experimental apparatus can be found in the literature [29]. Figure 5 compares the tangential velocity profiles obtained from the experiment and numerical simulation at different heights. The experimental

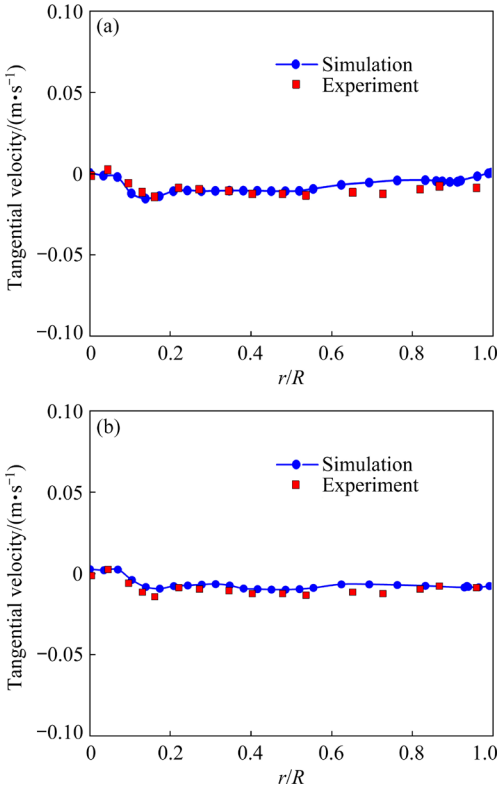

Fig. 5 Comparison of experimental [29] and simulation results for tangential velocity at heights of 30 mm (a) and 45 mm (b)

results are satisfactorily predicted by numerical model, and the characteristics of the velocity distribution of the fluid are nearly the same. The variation of the tangential velocity of the fluid is more manifest in the core region than that close to the sidewall.

4.2 Flow patterns

When the gas is introduced into the reactor through the lance, the vigorous chaotic motion of bubbles (e.g., formation, coalescence, growth, detachment, and eruption) certainly exerts a strong impact on the fluid hydrodynamics of the bath. To explore the relationship between the flow field and bubble motion, the distribution of the instantaneous velocity of fluid and the morphology of bubble in the central axial slice (x=0 mm) are depicted in Fig. 6. The velocity in this figure represents the averaged velocity of the mixtures of gas, slag, and copper matte over the x=0 mm section plane at each time instant. The volume fraction of the slag is presented at several time instants. The contour plots that represented the instantaneous distribution of slag volume fraction are depicted in the figure, in which the red and blue represent that the volume fractions of the slag are equal to 1 and 0, respectively. The period time of bubble behavior is defined as the summation of the waiting time and formation time by ZHANG et al [30]. In the current study, the period time is evaluated as the time difference between the moment of bubble formation and the bubble detachment because the waiting time is too small and can be neglected.

With the gas injection from the lance, the bubble is formed with an approximately spherical morphology at the exit of the submerged lance, attributed to the local balance of capillary and hydro-static pressures. Then, a mushroom-shaped void appears at the bottom of the bubble (t=0.1 s) due to the continuous injection of a large gas flow rate in the vertical direction. When the bubble volume exceeds the maximum tolerable value, the buoyancy induces the bubble to ascend. Simultaneously, a thin liquid layer occurs at the bubble boundary and a wave of the molten slag surface is captured. From 0.17 s, the symmetrical bubble rises to the free surface and erupts from the slag phase layer. As the process continues, the discharge of the bubble drives the splashing of the nearby slag phase. For the motion characteristics of the ternary mixture, the fluid velocity dramatically increases in the developed flow stage because of the bubble expansion. After that, the fluctuation of the fluid velocity can be observed, and the time-averaged velocity of the fluid is 0.497 m/s after reaching the pseudo-steady state. Besides, two main conclusions describing the correlation between the fluid velocity and bubble behavior are listed as

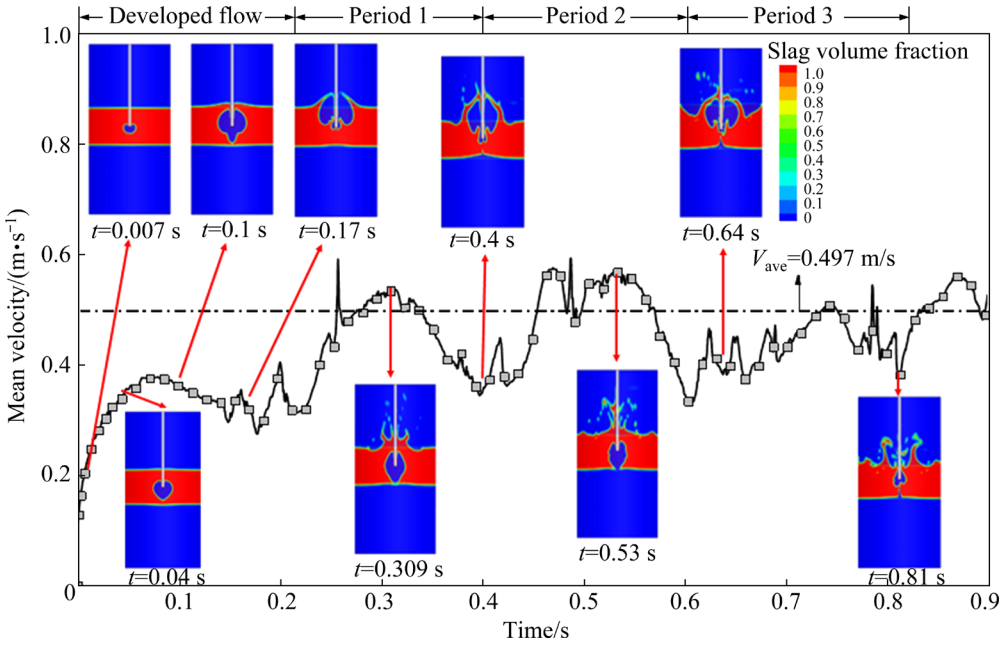

Fig. 6 Space−time distribution of fluid velocity and bubble formation process in central axial slice of x=0 m (V_g=67 m/s)

follows: (1) both temporal evolution of the bubble and fluid velocity are periodic; (2) the fluid velocity increases when the bubble is formed below the orifice, while the former gradually reduces when the bubble rises along the rim of the lance.

Figure 7 demonstrates the time-averaged temperature distribution of the fluid phase with a gas velocity of 67 m/s. After the gas is introduced into the reactor, the heat transfer between the ambient gas and slag phase increases the gas temperature. Thus, the non-uniform temperature distribution appears in the reactor. The temperature is low near the lance but high in the periphery region, and the temperature gradient is formed in the cross-sections (Fig. 7(a)). The low-temperature gas reduces the slag temperature but slightly affects the temperature of the copper matte (Fig. 7(b)). Besides, the discrepancy in the fluid temperature leads to the formation of V-shaped and W-shaped temperature distribution at the height of 0.43 and 0.52 m, respectively. The temperature difference along the radial direction at the height of 0.43 m is larger than that of 0.52 m, attributed to the bubble being heated by the high-temperature slag phase during the rising process (Figs. 7(c, d)).

4.3 Effect of gas injection velocity on flow field

In the practical operation, the mixing performance between gas and slag phases is enhanced by increasing the gas injection velocity. However, the high-velocity jet intensely promotes the momentum transfer from the gas to the copper matte phase and further affects the smelting efficiency. In this section, a series of gas velocities ranging from 58 to 94 m/s are adopted to investigate the effect of gas injection flow on the distribution of the fluid velocity and Q-criterion at different locations of the bath (the schematic of the locations is depicted in Fig. 8).

The Q-criterion, which is directly derived based on the second invariant Q of the velocity gradient tensor in the flow field, is adopted to identify the vortex structure with the following expression [31]:

$$Q=-\frac{1}{2}\left[\left(\frac{\partial u_x}{\partial x}\right)^2+\left(\frac{\partial u_y}{\partial y}\right)^2+\left(\frac{\partial u_z}{\partial z}\right)^2\right]-\frac{\partial u_x}{\partial y}\frac{\partial u_y}{\partial x}-\frac{\partial u_x}{\partial z}\frac{\partial u_z}{\partial x}-\frac{\partial u_y}{\partial z}\frac{\partial u_z}{\partial y} \tag{23}$$

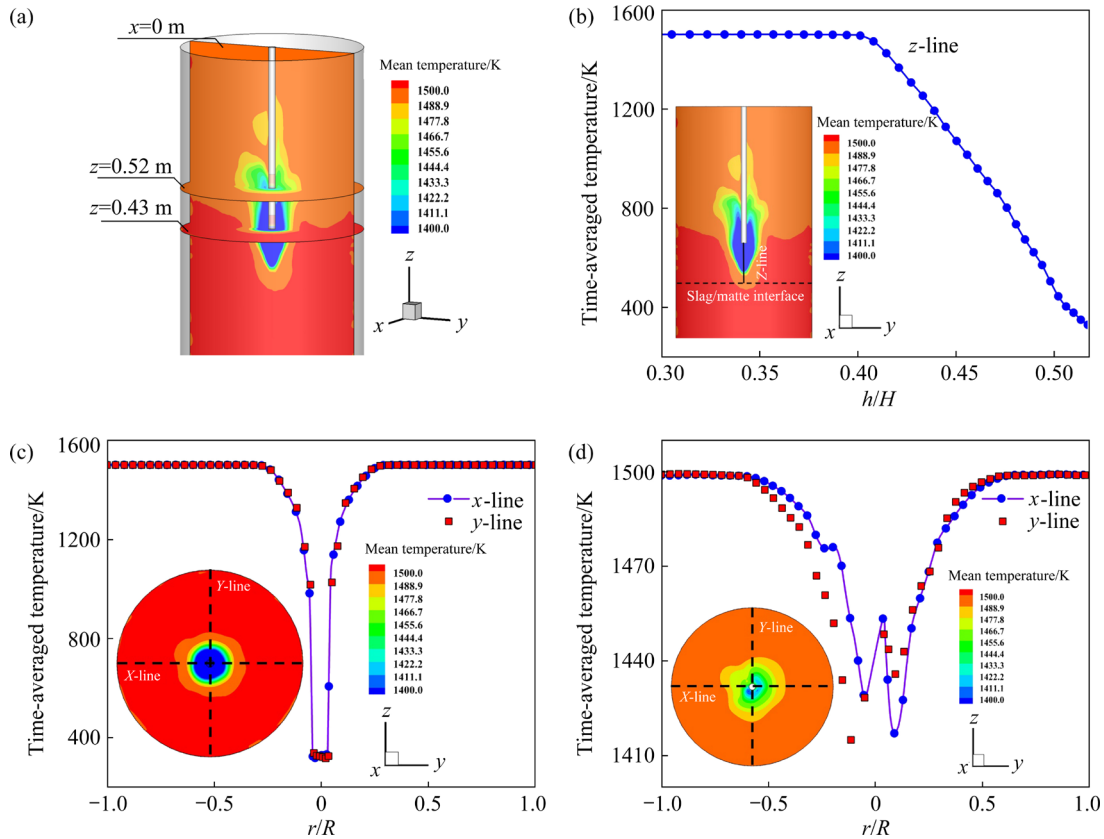

Fig. 7 Spatial distribution of time-averaged temperature of fluid (a); profiles of time-averaged temperature at different locations: (b) x=0 m; (c) z=0.43 m; (d) z=0.52 m (V_g= 67 m/s)

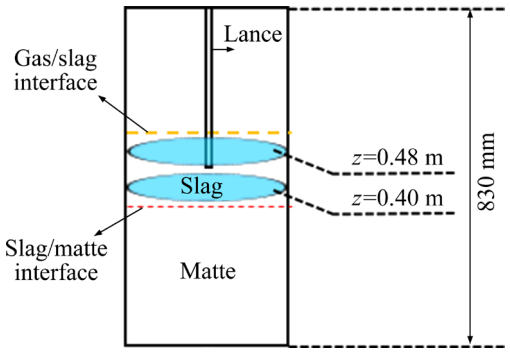

Fig. 8 Schematic of monitored surface in bath

When the threshold Q>0, the vorticity magnitude is greater than the magnitude of the strain rate, indicating the rotation or vortices dominated region of flow in this region [32,33]. Thus, the larger volume of thresholds Q-criterion represents the wider range of strong rotation of the fluid in the reactor. In the gas−liquid flow system, the intensity of the vortex varies with the positions. A specific threshold of the Q should be chosen to clearly visualize the vortex intensity in the reactor. In the present work, the iso-surface of the vortex appears in the entire slag phase layer and gas layer when a threshold Q of 50 s^{-2} is presented, while the vortex structure cannot be observed in the TSL reactor when a threshold Q of 50000 s^{-2} is chosen. To this end, the threshold Q of 5000 s^{-2} is set to identify the vortex structure in the reactor.

Figure S1 of Supporting Information indicates the effect of the gas injection rates on the time-averaged distribution of the radial velocity of the fluid at two different height cross-sections. The location of the monitored cross-sections (i.e. z=0.40 m and z=0.48 m) is shown in Fig. 8. The fluid velocity gradually reduces from the core region to the sidewall due to the consumption of the kinetic energy but increases with the gas velocity due to the vigorous momentum transfer between the gas and slag phases. Moreover, the effective disturbance range of bubbles to the slag phase is 0.08 m under different vertical gas velocities, indicating that the impact of gas velocity on the lateral distribution is limited.

Figure 9 shows the effect of gas injection velocity on the threshold Q-criterion and slag phase volume fraction. The green represents the iso-vortex surface with a Q-criterion value of 5000 s^{-2}, and red denotes the gas/slag interface that a threshold slag phase volume fraction is equal to 0.95. The gas/slag interface observed in the figure can also represent the morphology of the bubble. Numerous irregular vortices appear in the proximity of the lance with the wave of the molten slag surface, demonstrating that part of the gas phase has overflowed the free surface without fully stirring the liquid phase, and the momentum transfer process between the gas and slag phases is not completely proceeded. The vertical penetration depth of the bubble and volume of the high vorticity region are significantly impacted by gas velocity. Specifically, the influence of bubbles on the copper matte phase can be neglected when the gas injection velocity is 58 m/s. With enlarging the gas flow rate, the gas penetration depth in slag phase increases. When the gas is injected into the slag layer with a velocity of 94 m/s, the copper matte is stirred by the gas, which results in the mixing of the slag and copper matte and adversely impacts the quality of the product in the actual operation. Besides, the volume of the strong rotation region enlarges with the superficial gas velocity.

Instantaneous and time-averaged distribution of gas penetration depth is presented to explore the influence of the gas injecting velocity on the

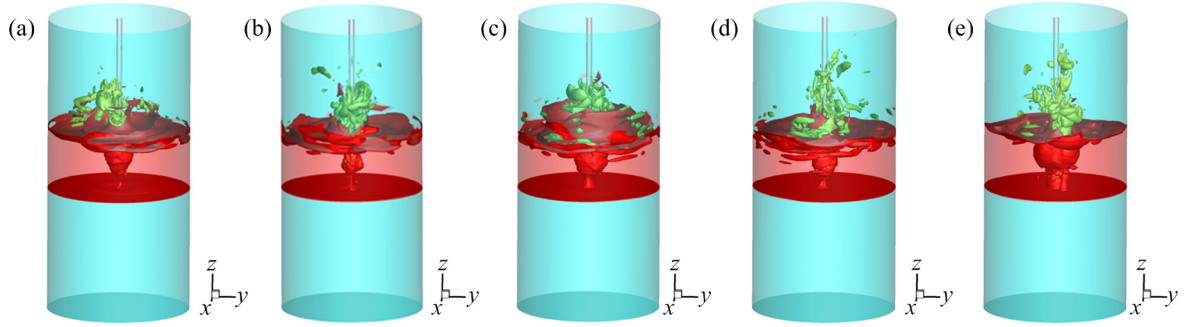

Fig. 9 Spatial distributions of iso-surface of volume fraction of slag phase (φ_{slag}=0.95) and vortex flow structures (Q=5000 s^{-2}) with different gas injection velocities: (a) 58 m/s; (b) 67 m/s; (c) 76 m/s; (d) 85 m/s; (e) 94 m/s

penetration performance inside the slag layer, as shown in Fig. 10. For all the explored cases, the gas penetration depth initially increases from zero and then fluctuates around a fixed value. The gas penetration depth increases with the superficial velocity, which is attributed to the increase of the inertial force of gas phase. The gas injection with the velocity of 96 m/s leads to approximately 78.4% and 31.9 % increase in the time-averaged and maximum penetration depth compared with that of 58 m/s, respectively. Nevertheless, the maximum gas penetration depths in the liquid with the injection velocity of 76, 85, and 94 m/s are larger than the distance between the orifice and slag-matte interface, indicating that the copper matte phase is disturbed by the bubble.

4.4 Effect of swirling flow on flow field

As reported in the open literature, the swirling gas flow enhances the mean convective mixing efficiency and minimizes the splashes of the liquid melt [34,35]. To elucidate the impact of the swirling flow on the in-furnace flow field, three swirling flow conditions (namely, Case SF1, Case SF2, and Case SF3) and one gas vertically-injecting condition (namely, Case VF) are simulated. All the simulated cases are set with the same injection velocity (V_g=67 m/s). The swirl velocity of the gas at the orifice contains three noticeable azimuthal components (i.e., axial, radial, and tangential velocity components). The details of these velocity components are listed in Table 2.

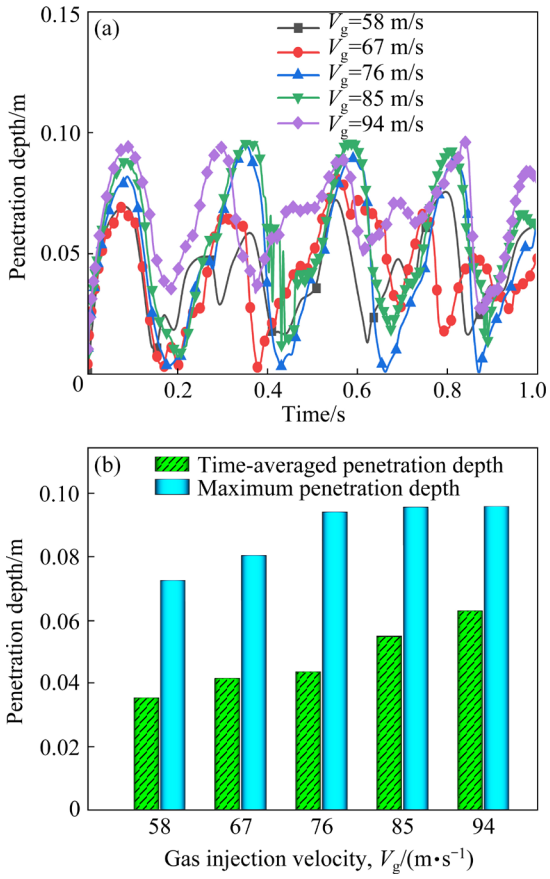

Fig. 10 Temporal evolution of gas penetration depth in liquid phase (a); histogram of time-averaged and maximum penetration depth of gas under different injection velocities (b)

Table 2 Details of velocity component magnitude with different conditions

Case	Total velocity/ (m·s^{-1})	Axial velocity/ (m·s^{-1})	Tangential velocity/ (m·s^{-1})	Radial velocity/ (m·s^{-1})
SF1	67	−60.3	27.42	10.05
SF2	67	−62.53	23.40	5.58
SF3	67	−64.99	16.25	1.12
VF	67	−67	0	0

Figure S2 of Supporting Information illustrates the effect of the swirling flow on the time-averaged distribution of the radial velocity of the fluid at the height of 0.40 and 0.48 m. The fluid velocity for Case VF is higher than that for the swirling flow cases at height of 0.40 m, while the fluid velocity of these several conditions is the same at the height of 0.48 m. Moreover, the time-averaged velocity of the fluid for the Case SF1 is the largest, followed by the Case SF2, and the velocity under the Case SF3 is the lowest.

Figure 11 demonstrates the effect of swirling flow on the threshold Q-criterion and slag phase volume fraction. The vortex for the swirling flow cases is visibly lower than that for Case VF. It is indicated that the centrifugal force of the swirling flow promotes the agitation performance of the gas in the slag phase, and most of the gas momentum is transferred to the slag phase. The fluctuation of the molten slag surface and splashing of slag phase in the swirling flow cases is weaker than that in the Case VF due to the radial and tangential stirring effect of the swirling flow. Moreover, the bubble volume increases with the tangential velocity component of swirling flow, attributed to the enhancement of the disturbance in the horizontal direction. The disturbance of the gas phase to the copper matte is insignificant in the swirling flow cases.

Figure 12 denotes the contour plots of the fluid vorticity in a central slice x=0 mm and three horizontal cross-sections (z=0.43, 0.52, 0.65 m). Due to the vigorous motion of the gas phase, the distribution of the vorticity is non-uniform in the reactor, and the high vorticity is mainly concentrated in the core region of the slag phase and the region above the molten slag surface. For the swirling flow cases, the volume of the fluid with large vorticity in the vertical direction and lateral direction enlarges with the axial velocity and circumferential velocity, respectively. The volume of the large vorticity above the molten slag surface is smaller in the swirling flow cases than that in Case VF, indicating that the momentum transfer efficiency between the phases under the swirling flow condition is higher than that under the gas vertically-injecting condition.

Figure 13 represents the instantaneous distribution of the lateral chord length and the vertical penetration depth of the bubble. The fluctuation of the lateral chord length of the bubble is more complicated than that of the vertical penetration depth for the swirling flows. Moreover, the lateral chord length of the bubble is manifestly larger than the gas penetration depth due to the buoyancy of gas phase. It is indicated that the swirling flows enhance the non-linear mixing of the

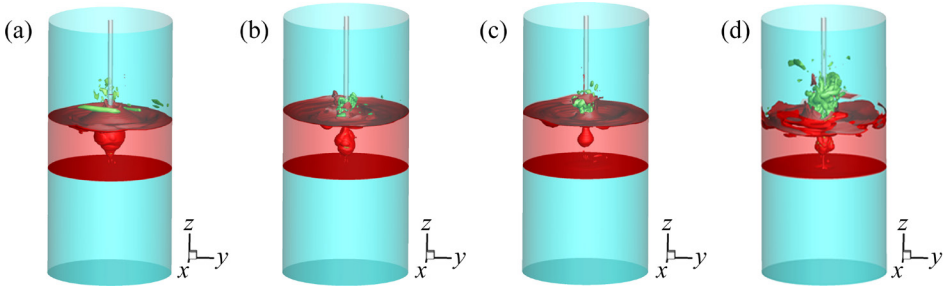

Fig. 11 Spatial distribution of iso-surface of slag phase volume fraction ($\varphi_{\text{slag phase}}$=0.95) and vortex flow structures based on Q-criterion (with Q=5000 s^{-2}): (a) Case SF1; (b) Case SF2; (c) Case SF3; (f) Case VF

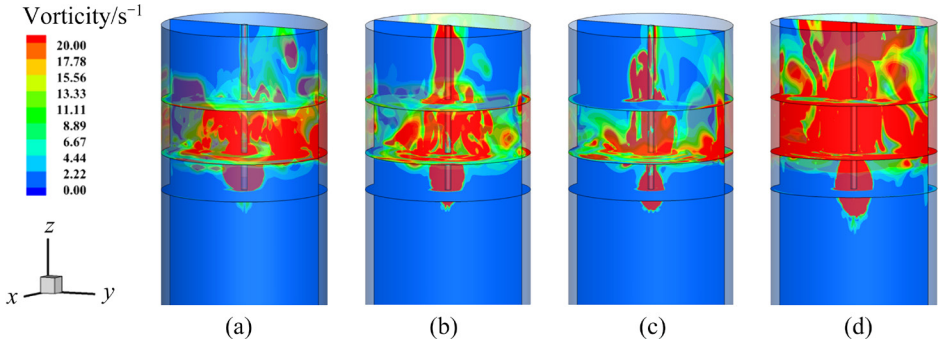

Fig. 12 Contour plots of fluid vorticity at time of 1 s: (a) Case SF1; (b) Case SF2; (c) Case SF3; (d) Case VF

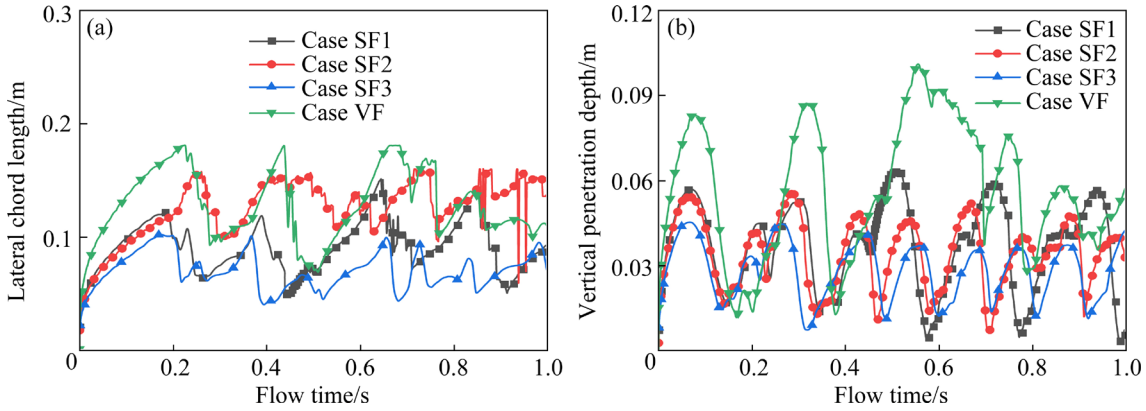

Fig. 13 Time evolution of lateral chord length (a) and vertical penetration depth (b) of bubble

gas and around still slag, and the tangential velocity component improves the momentum transfer efficiency between gas and slag phases.

In the TSL process, the stirring intensification of the gas to slag is determined by the penetration depth and lateral chord length of the bubble. The disturbance ranges of the bubble increase with the bubble size. Specifically, the flat-shape bubble enhances the lateral turbulence intensity of the liquid, while the bubble with a stretched shape manifest increases the stirring performance of the gas in the vertical direction. To quantify the influence of the swirling flow on the bubble shape, the bubble aspect ratio (Ψ_{xz}) is introduced as a dimensionless variable and can be derived as follows:

$$\Psi_{xz} = L_x / L_z \tag{24}$$

where L_x, and L_z are the lateral and vertical chord lengths of the bubble, respectively.

Figure 14 presents the effect of swirling flow on the bubble aspect ratio when the bubble expands to the maximum volume during the steady growth process. For the swirling flow, the lowest aspect ratio of the bubble with a value of 0.835 is observed in Case SF3, indicating that the bubble chord length in the vertical direction is significantly larger than that in the lateral direction. But the bubble aspect ratio is enlarged when the circumferential velocity component increases, attributed to the strengthened stirring effect of the gas in the lateral direction. Besides, the bubble aspect ratio of Case SF2 is approximately equal to that of Case VF, while the bubble aspect ratio of Case SF3 is lower than that of Case VF. This means that a smaller circumferential velocity component adversely affects the lateral disturbance of the bubble.

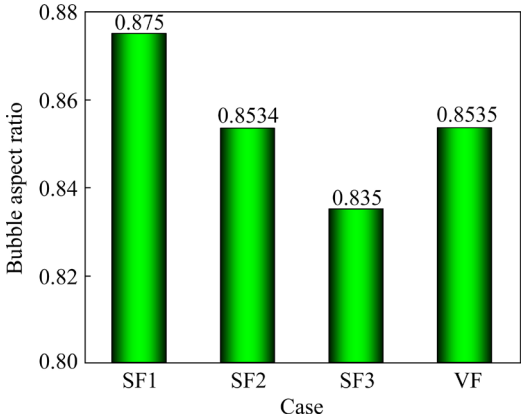

Fig. 14 Effect of swirling flow on bubble aspect ratio

5 Conclusions

(1) The bubble is initially formed with an approximately spherical shape but then a protruding shape is observed in the bubble tail. The formation and rising of the bubble increase and reduce the fluid velocity, respectively. The low-temperature gas injected from the orifice induces the V-shaped and W-shaped temperature distributions of the fluid at the height of 0.43 and 0.52 m, respectively.

(2) When the bubble drives liquid to ascend, the high gas velocity region is concentrated in the core region. Higher nitrogen velocity increases the gas penetration depth in the slag phase and gas vortices above the molten slag surface. Compared to the gas injecting velocity of 58 m/s, the time-averaged and maximum gas penetration depth with the gas injecting velocity of 94 m/s are increased by 78.4% and 31.9%, respectively.

(3) Swirling flow effectively suppresses the slag splashing and enhances the momentum transfer efficiency between phases. For the swirling flow, the instantaneous distribution of the lateral chord length of the bubble is larger than that of the vertical penetration depth. Besides, the aspect ratio of the bubble for Case VF is lower than that for Case SF1 but larger than that of the other swirling flow cases.

Acknowledgments

The authors thank the financial support from the Applied Basic Research Project of Yunnan Province, China (No. 202301AT070411), and the Analysis and Testing Foundation of Kunming University of Science and Technology, China (No. 2021P20191102002).

Supporting Information

Supporting Information in this paper can be found at: http://tnmsc.csu.edu.cn/download/21-p2231-2022-0200-Supporting_Information.pdf.

Nomenclatures

D_ω^+ Positive portion of shear-stress transport cross-diffusion term, kg/(m·s^2)

$\boldsymbol{F}_{\mathrm{ST}}$ Surface tension force, N/m

$\boldsymbol{g}$ Gravitational acceleration, m/s^2

k Turbulence kinetic energy, m^2/s^2

p Fluid pressure, Pa

P_k Production of turbulence kinetic energy, kg/(m·s^3)

P_ω Production of specific dissipation rate, kg/(m^3·s^2)

Re Reynolds number

S Absolute value of strain rate, s^{-1}

S_{ij} Rate-of-strain, s^{-1}

t Time instant, s

$\boldsymbol{u}$ Fluid velocity, m/s

α Fluid volume fraction

α^* Damping coefficient

μ Fluid viscosity, kg/(m·s)

μ_t Turbulent viscosity, kg/(m·s)

ρ Fluid density, kg/m^3

σ_k Turbulent Prandtl number for turbulence kinetic energy

σ_ω Turbulent Prandtl number for specific dissipation rate

ω Specific dissipation rate, s^{-1}

Ψ Bubble aspect ratio

β_*, β_1, β_2, a_1 Closure coefficients in SST turbulence model

References

[1] WU Ying-dong, LIU Zhong-qiu, LI Bao-kuan, GAN Yong. Numerical simulation of multi-size bubbly flow in a continuous casting mold using population balance model [J]. Powder Technology, 2022, 396: 224−240.

[2] SHEN Xiu-zhong, HIBIKI T. Distribution parameter and drift velocity for upward gas-liquid metal two-phase flow [J]. Applied Thermal Engineering, 2021, 184: 116242.

[3] CHEN Zhi-bin, YAN Hong-jie, ZHOU Ping, YANG Ping, DING Jie-hui, LIU Jia, LIU Liu. Parametric study of gas-liquid two-phase flow field in horizontal stirred tank [J]. Transactions of Nonferrous Metals Society of China, 2021, 31(6): 1806−1817.

[4] LIU Chang, LI Xin, SHU Shi, HUANG Yu-he, LI Xing-gang, ZHU Qiang. Numerical investigation on flow process of liquid metals in melt delivery nozzle during gas atomization process for fine metal powder production [J]. Transactions of Nonferrous Metals Society of China. 2021, 31(10): 3192−3204.

[5] WANG Peng, LI Jing, WANG Xin, LIU Heng-San, FAN Bin, GAN Ping, GUO Rui-Feng, GE Xue-Yuan, WANG Miao-Hui. Close-coupled nozzle atomization integral simulation and powder preparation using vacuum induction gas atomization technology [J]. Chinese Physics B, 2021, 30(2): 27502.

[6] GHADIMI REZAEI M, HASHEMI TARI P, EMAMZADEH M, TAFAGHODI KHAJAVI L. 3D numerical investigation of effects of density and surface tension on mixing time in bottom-blown gas-stirred ladles [J]. Transactions of Nonferrous Metals Society of China, 2021, 31(10): 3177−3191.

[7] YAN Hong-jie, XIAO Jun-bing, SONG Yan-po, HU Zhi-wen, TAN Zhi-kai, LIU Liu. Cold model on bubble growth and detachment in bottom blowing process [J]. Transactions of Nonferrous Metals Society of China, 2019, 29(1): 213−221.

[8] WIJENAYAKE J J, SOHN H S. The synthesis of tire grade ZnO from top submerged lance (TSL) furnace flue dust generated in Cu recycling industries [J]. Hydrometallurgy, 2020, 198: 105466.

[9] OBISO D, REUTER M, RICHTER A. CFD investigations of bath dynamics in a pilot-scale TSL furnace [J]. Metallurgical and Materials Transactions B: Process Metallurgy and Materials Processing Science, 2021, 52(8): 3064−3077.

[10] KOLCZYK E, MICZKOWSKI Z, CZERNECKI J. Influence of selected parameters on phenomena of two-phase flow and heat exchange in TSL furnace-numerical investigation [J]. International Journal of Numerical Methods for Heat & Fluid Flow, 2017, 27(12): 2799−2815.

[11] WANG Yan-nan, CAO Ling-ling, VANIERSCHOT M, CHENG Zhong-fu, BLANPAIN Bart, GUO Mu-xing. Modelling of gas injection into a viscous liquid through a top-submerged lance [J]. Chemical Engineering Science, 2020, 212: 115359.

[12] RODRIGUES H T, ALMEIDA A R, BARRIONUEVO D C, FRAGA R S. Effect of the gas injection angle and configuration in the efficiency of gas lift [J]. Journal of Petroleum Science and Engineering, 2021, 198: 108126.

[13] ZHAO Hong-liang, WANG Jing-qi, ZHANG Wan-long, XIE Mingzhuang, LIU Feng-qin, CAO Xiao-chang. Bubble motion and interfacial phenomena during bubbles crossing liquid−liquid interfaces [J]. Processes, 2019, 7(10): 719.

[14] KOVÁTS P, THÉVENIN D, ZÄHRINGER K. Influence of viscosity and surface tension on bubble dynamics and mass transfer in a model bubble column [J]. International Journal of Multiphase Flow, 2020, 123: 103174.

[15] OBISO D, KRIEBITZSCH S, REUTER M, MEYER B. The importance of viscous and interfacial forces in the hydrodynamics of the top-submerged-lance furnace [J]. Metallurgical and Materials Transactions B: Process Metallurgy and Materials Processing Science, 2019, 50(6): 3125.

[16] AKASHI M, KEPLINGER O, SHEVCHENKO N, ANDERS S, REUTER M A, ECKERT S. X-ray radioscopic visualization of bubbly flows injected through a top submerged lance into a liquid metal [J]. Metallurgical and Materials Transactions B: Process Metallurgy and Materials Processing Science, 2020, 51(1): 124−139.

[17] LIOW J L. Quasi-equilibrium bubble formation during top-submerged gas injection [J]. Chemical Engineering Science, 2000, 55(20): 4515−4524.

[18] WANG Yu-hui, WANG Shi-bo, WEI Yong-gang, ZHANG Ti-fu, LI Shi-wang. Numerical simulation of gas-liquid mixed top blowing to enhance momentum diffusion [J]. Applied Thermal Engineering, 2020, 181: 115971.

[19] OBISO D, AKASHI M, KRIEBITZSCH S, MEYER B, REUTER M, ECKERT S, RICHTER A. CFD modeling and experimental validation of top-submerged-lance gas injection in liquid metal [J]. Metallurgical and Materials Transactions B: Process Metallurgy and Materials Processing Science, 2020, 51(4): 1509−1525.
[20] WANG Yan-nan, VANIERSCHOT M, CAO Ling-ling, CHENG Zhong-fu, BLANPAIN B, GUO Mu-xing. Hydrodynamics study of bubbly flow in a top-submerged lance vessel [J]. Chemical Engineering Science, 2018, 192: 1091−1104.
[21] DONG Fei, WANG Zhi-ming, CAO Tao-tao, NI Jie. A novel interphase mass transfer model toward the VOF simulation of subcooled flow boiling [J]. Numerical Heat Transfer Part A: Applications, 2019, 76(4): 220−231.
[22] BRACKBILL J U, KOTHE D B, ZEMACH C. A continuum method for modeling surface tension [J]. Journal of Computational Physics, 1992, 100(2): 335−354.
[23] MENTER F R. Two-equation eddy-viscosity turbulence models for engineering applications [J]. AIAA Journal, 1994, 32(8): 1598−1605.
[24] ZHAO Hong-liang, YIN Pan, ZHANG Li-feng, WANG Sen. Water model experiments of multiphase mixing in the top-blown smelting process of copper concentrate [J]. International Journal of Minerals, Metallurgy, and Materials, 2016, 23(12): 1369−1376.
[25] ZHAO Hong-liang, LU Ting-ting, LIU Feng-qin, YIN Pan, WANG Sen. Computational fluid dynamics study on a top-blown smelting process with lance failure in an isa furnace [J]. JOM, 2019, 71(5): 1643−1649.
[26] WANG Dong-xing, LIU Yan, ZHANG Zi-mu, ZHANG Ting-an, LI Xiao-long. PIV measurements on physical models of bottom blown oxygen copper smelting furnace [J]. Canadian Metallurgical Quarterly, 2017, 56(2): 221−231.
[27] SHAO Pin, JIANG Le-peng. Flow and mixing behavior in a new bottom blown copper smelting furnace [J]. International Journal of Molecular Sciences, 2019, 20(22): 5757.
[28] MA Xiao-jian, HUANG Biao, LI Yi-kai, CHANG Qing, QIU Si-cong, SU Zheng, FU Xiao-ying, WANG Guo-yu. Numerical simulation of single bubble dynamics under acoustic travelling waves [J]. Ultrasonics Sonochemistry, 2018, 42: 619−630.
[29] MORSI Y S, YANG W, CLAYTON B R, GRAY N B. Experimental investigation of swirl and non-swirl gas injections into liquid baths using submerged vertical lances [J]. Canadian Metallurgical Quarterly, 2000, 39(1): 87−98.
[30] ZHANG Jian, YU Yong, QU Chen, ZHANG Yu. Experimental study and numerical simulation of periodic bubble formation at submerged micron-sized nozzles with constant gas flow rate [J]. Chemical Engineering Science, 2017, 168: 1−10.
[31] da SILVA C B, PEREIRA J C F. Invariants of the velocity-gradient, rate-of-strain, and rate-of-rotation tensors across the turbulent/nonturbulent interface in jets [J]. Physics of Fluids, 2008, 20(5): 055101.
[32] BANKO A J, EATON J K. A frame-invariant definition of the *Q*-criterion [R]. Center for Turbulence Research Annual Research Briefs, 2019: 181−194.
[33] ZHAN Jie-min, LI Yu-tian, WEI Yong-kang. Comparison between the *Q* criterion and Rortex in the application of an in-stream structure [J]. Physics of Fluids, 2019, 31(12): 121701.
[34] HUDA N, NASER J, BROOKS G, REUTER M A, MATUSEWICZ R W. CFD modeling of swirl and nonswirl gas injections into liquid baths using top submerged lances [J]. Metallurgical and Materials Transactions B: Process Metallurgy and Materials Processing Science, 2010, 41(1): 35−50.
[35] ZHAO Hong-liang, LU Ting-ting, YIN Pan, MU Liang-zhao, LIU Feng-qin. An experimental and simulated study on gas−liquid flow and mixing behavior in an ISASMELT furnace [J]. Metals, 2019, 9(5): 565.

顶吹浸没熔炼炉中气–渣–铜锍多相流搅拌特性的数值模拟

万章豪[1]，杨世亮[1]，孔德颂[2]，李东波[2]，胡建杭[1]，王 华[1]

1. 昆明理工大学 复杂有色金属资源清洁利用国家重点实验室，昆明 650093；
2. 云南铜业股份有限公司 西南铜业分公司，昆明 650102

摘 要：采用 VOF 方法对顶吹浸没熔池中氮气–渣–铜锍的流体动力学特性和搅拌特性进行数值研究。阐明气泡行为和流体速度之间的关系；研究气体入射速度和旋流对流体涡流结构、气体穿透深度和流体速度的影响。结果表明，气泡的形成和上升分别增加和降低流体速度。由于低温气体的注入，流体温度在高度 0.43 m 和 0.52 m 处分别呈现 V 形和 W 形分布。相比于 58 m/s 的气体注入速度，气速为 98 m/s 时气相的时均和最大穿透深度分别增加 78.4%和 31.9%。由于轴向速度分量的减小，旋流降低气体穿透深度、增加相间动量传递效率、抑制渣相喷溅。

关键词：顶吹浸没喷枪；气泡行为；旋流；多相流；氮气–渣–铜锍

(Edited by Bing YANG)